# Enhanced Climate Change and Its Detection over the Rocky Mountains

JOHN C. FYFE AND GREGORY M. FLATO

*Canadian Centre for Climate Modelling and Analysis, Atmospheric Environment Service, Victoria, British Columbia, Canada*

(Manuscript received 5 August 1997, in final form 19 February 1998)

ABSTRACT

Results from an ensemble of climate change experiments with increasing greenhouse gas and aerosols using the Canadian Centre for Climate Modelling and Analysis Coupled Climate Model are presented with a focus on surface quantities over the Rocky Mountains. There is a marked elevation dependency of the simulated surface screen temperature increase over the Rocky Mountains in the winter and spring seasons, with more pronounced changes at higher elevations. The elevation signal is linked to a rise in the snow line in the winter and spring seasons, which amplifies the surface warming via the snow-albedo feedback. Analysis of the winter surface energy budget shows that large changes in the solar component of the radiative input are the direct consequence of surface albedo changes caused by decreasing snow cover.

Although the warming signal is enhanced at higher elevations, a two-way analysis of variance reveals that the elevation effect has no potential for early climate change detection. In the early stages of surface warming the elevation effect is masked by relatively large noise, so that the signal-to-noise ratio over the Rocky Mountains is no larger than elsewhere. Only after significant continental-scale warming does the local Rocky Mountain signal begin to dominate the pattern of climate change over western North America (and presumably also the surrounding ecosystems and hydrological networks).

## 1. Introduction

Giorgi et al. (1997, hereafter GHMB) identified an elevation dependency of the Alpine surface climate change signal in the National Center for Atmospheric Research (NCAR) Regional Climate Model. The regional model was driven at its lateral boundaries by output from NCAR Community Climate Model ''present-day'' and doubled carbon dioxide runs. Plots of the change in surface temperature between the regional model present-day and $2 \times CO_2$ runs showed a marked dependency on elevation, with more pronounced warming at higher elevations, especially so in the winter and spring seasons. Corresponding changes with elevation of snow depth and absorbed solar flux at the surface pointed directly to the snow-albedo feedback as the underlying mechanism. The observational study of Beniston and Rebetez (1996) supports this model result.

GHMB speculated that the elevation signal had been overlooked in general circulation model (GCM) studies because the coarse-resolution topographies of GCMs (circa 1995, when the paper was first written) were too smooth for the effect to be detected. They took as their example the R15 NCAR GCM topography, which represents the Alps as a 400-m mound—presumably too stunted for a topographically induced climate change signal to be present. The Alps are certainly underestimated in GCMs (and especially so at R15 resolution, which is quite coarse by current standards), but other mountain complexes, such as the Rockies, are much less so. Figure 1 compares the topography of western North America with that of the Canadian Centre for Climate Modelling and Analysis (CCCma) T32 Coupled Climate Model. Of course, the model topography does not capture all of the ''details'' of the Rockies but it does, as we shall see, reach high enough over a large enough area to support appreciable winter and springtime snow cover—the essential ingredient for the elevation effect put forward by GHMB. Indeed, we will demonstrate that the Rocky Mountains in a transient climate change simulation using the CCCma Coupled Climate Model drive a locally enhanced climate change signal that dominates the pattern of change over western North America. Further, and going beyond GHMB, we will characterize the temporal evolution of the elevation signal, as well as the complete surface energy balance with which it is associated. The temporal information provided by a transient climate change simulation allows us to assess the potential of the elevation signal as a tool for early climate change detection.

Section 2 describes of the CCCma Coupled Climate Model, the set of experiments to be analyzed, and the methods of analysis. Section 3 contains our main results. Section 3a establishes the elevation effect and its relationship with other variables in the model. Section 3b

*Corresponding author address:* Dr. John Fyfe, Canadian Centre for Climate Modelling and Analysis, Atmospheric Environment Service, University of Victoria, Victoria, BC V8W 2Y2 Canada.
E-mail: John.Fyfe@ec.gc.ca

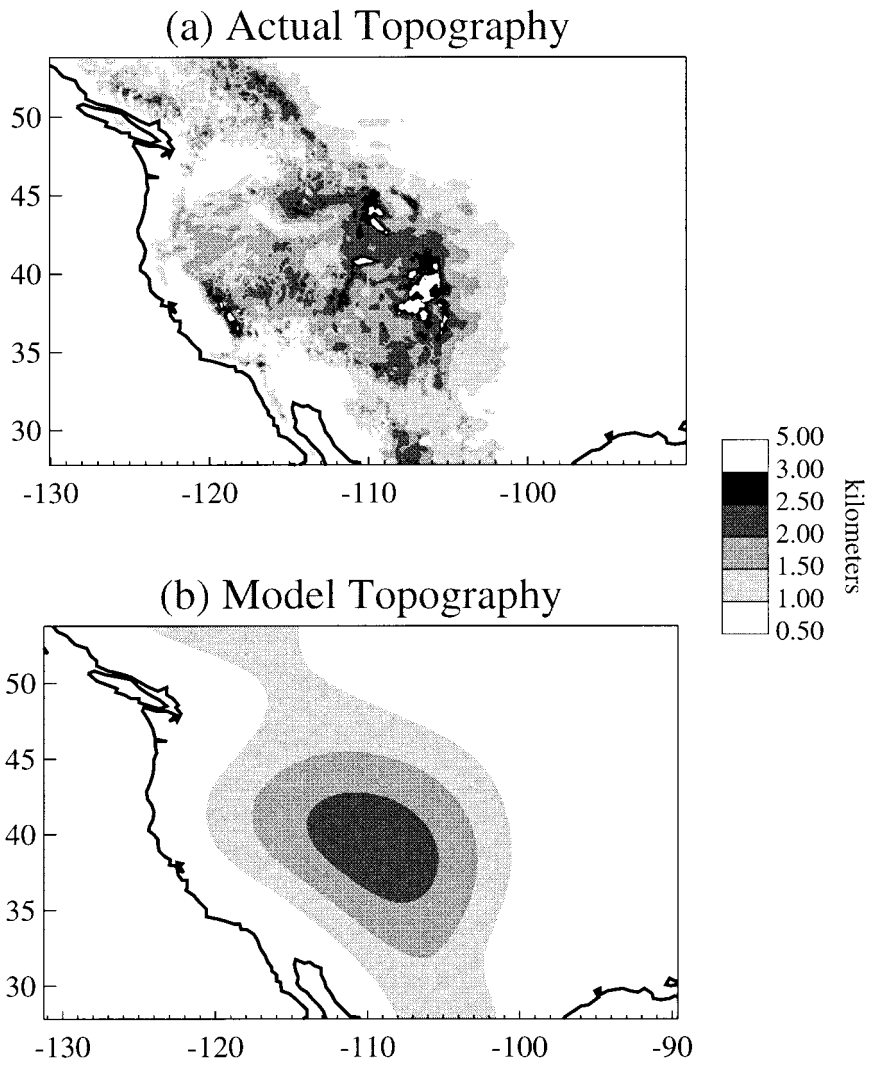


FIG. 1. Western North American topography (units are km): (a) (1/6)° lat × (1/6)° long resolution. (b) Topography used in the T32 CCCma Coupled Climate Model.

describes the mechanism behind the effect via a detailed analysis of the surface energy budget. Section 3c quantifies its potential for early climate change detection. Section 4 completes the paper with a brief summary and concluding remarks.

## 2. Model description and analysis procedures

### *a. Model description*

The results analyzed in this paper were obtained from the first version of the CCCma Coupled Climate Model (CGCM1). The atmospheric portion of the model is a spectral model with triangular truncation at wavenumber 32, and 10 unequally spaced levels in the vertical. This model is essentially that described by McFarlane et al. (1992, hereafter referred to as MBBL) and Boer et al. (1992). The snow and albedo parameterizations are more or less standard. Precipitation is assumed to fall as snow if the screen-level air temperature is less than or equal to the freezing point. The snow-albedo parameterization accounts for the decrease in albedo with snow age (computed prognostically), and the effect of partial snow cover and vegetation masking. The latter effect is represented by a linear combination of snow-covered and snow-free albedos until the snow reaches a so-called masking depth specified from the land surface dataset of Wilson and Henderson-Sellers (1985). The result is that surface albedo is a nonlinear function of snow depth. As shown in Flato et al. (1998, manuscript submitted to *Climate Dyn.*) the CGCM1 wintertime snow cover over the Rockies compares quite well with observations.

The ocean component of the model is based on the Geophysical Fluid Dynamics Laboratory MOM-1 code

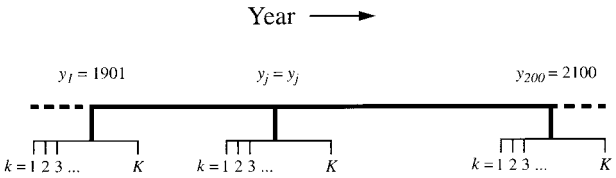


FIG. 2. Schematic diagram of the data processing procedure. The dashed line represent the years for which the time series were extrapolated in order to obtain *K*-yr central running averages.

(Pacanowski et al. 1991) and has a horizontal resolution of 1.875°, with 29 unevenly spaced levels in the vertical. Prior to coupling, the ocean and atmosphere models are individually integrated to their respective equilibria. Monthly flux adjustment fields for heat and freshwater are computed from these equilibria and then further refined by running the coupled model with weak restoring terms on sea surface temperature and salinity for an additional 14 yr. These flux adjustments are held fixed for the subsequent control and transient simulations. A more detailed description of the model, its control climate, and the spinup–flux-adjustment scheme is given by Flato et al. (1998, manuscript submitted to *Climate Dyn.*).

The transient climate change simulations discussed here follow the approach used by Mitchell et al. (1995), wherein the effective greenhouse gas forcing change corresponds to that observed from 1850 to the present, with a forcing change corresponding to an increase of $CO_2$ at a rate of 1% $yr^{-1}$ (compounded) thereafter until the end of the simulation in year 2100. The direct forcing effect of sulfate aerosols is included by increasing the surface albedo in an appropriate manner (Reader and Boer 1998) based on loadings from the sulfur cycle model of Langner and Rodhe (1991). Three independent realizations of the simulated transient climate change are available and have been analyzed in some detail by Boer et al. (1998a, manuscript submitted to *Climate Dyn.*; 1998b, manuscript submitted to *Climate Dyn.*); we use results from these three realizations here.

### *b. Data processing and analysis procedures*

Our starting point is an archive of monthly means for the period from March 1901 to February 2100. For each surface variable and realization we obtain four seasonal mean time series—December–February, March–May, June–August, September–November (DJF, MAM, JJA, SON, respectively)—containing 200 fields each. To prepare for computing a central running average for each time, we used autoregressive forecasting and backcasting to extrapolate the time series (as indicated by the horizontal dashed lines in Fig. 2). Letting $T_{ijk}$ denote the seasonal mean screen temperature of the $k$th yr ($k = 1, \ldots, K$) in the $j$th period ($j = 1, \ldots, 200$) in the $i$th realization ($i = 1, \ldots, I$), we use $\overline{T}_{ij.}$ and $s^2_{ij.}(T)$ to denote the $K$-yr central running seasonal mean and variance for the $i$th realization; that is,

$$\overline{T}_{ij.} \equiv \frac{1}{K}\sum_k T_{ijk} \quad \text{and} \quad s^2_{ij.}(T) \equiv \frac{1}{(K-1)}\sum_k (T_{ijk} - \overline{T}_{ij.})^2, \tag{1}$$

where the central year of the $j$th period is $j + 1900$, and we will henceforth refer to the $K$-yr period centered on this year as $y_j = j + 1900$. The climate signal for period $y_j$ is defined as the ensemble-averaged $\overline{T}_{ij.}$; that is,

$$[T]_{y_j} \equiv \frac{1}{I}\sum_i \overline{T}_{ij.}. \tag{2}$$

The climate signal *change* between period $y_j$ and a fixed reference period $y_{j^*}$ is

$$\delta_{y_j}[T] \equiv [T]_{y_j} - [T]_{y_{j^*}}, \tag{3}$$

with the asterisk always denoting the fixed reference period.

When discussing climate change, and specifically climate change detection, issues of statistical significance are unavoidable. A *t*-test procedure assesses the equality of the $y_j$ and $y_{j^*}$ period climate signals by first defining a pooled ensemble mean variance $s_p^2 = (1/I)\,\Sigma_i\,(s^2_{ij.} + s^2_{ij^*.})/2$ and then computing the $t$ statistic,

$$t_0[T] \equiv \delta[T]/\sigma[T], \tag{4}$$

where $\sigma[T] = \sqrt{2s_p^2/IK}$ is an estimate of the standard deviation of the difference of ensemble means, which we will refer to simply as the ''standard deviation.'' At the $\eta$ significance level we reject the null hypothesis that the $y_j$ and $y_{j^*}$ climate signals are equal if $|t_0| > t_{\eta/2,2I(K-1)}$, where $t_{\eta/2,2I(K-1)}$ is the upper $\eta/2$ percentage point of the $t$ distribution with $2I(K-1)$ degrees of freedom. We note that this test procedure assumes equality of the $y_j$ and $y_{j^*}$ period ensemble-mean variances, which we have determined to be an excellent assumption throughout. In what follows we set $K = 11$, the reference period $y_{j^*}$ is centered on year 1915, and $\eta = 1\%$. We have experimented extensively with different values of averaging-length $K$, reference period $y_{j^*}$, and significance level $\eta$ and found little change in the basic results. For these settings, $t_{\eta/2,2I(K-1)} \approx 2.4$, so we see that a climate signal change greater than about 2.4 times the standard deviation is significant.

## 3. Results

### *a. The enhanced climate change signal*

Figure 3 displays the spatial distribution of $\delta_{2095}[T]$ for each season (the bold curve in each plot is the 1.5-km elevation contour). In DJF (and to a lesser extent, MAM) there is a large climate change signal that is clearly collocated with high elevation (note the location of the 1.5-km elevation contour). Indeed, it is the ''bull's-eye'' of enhanced climate change signal seen

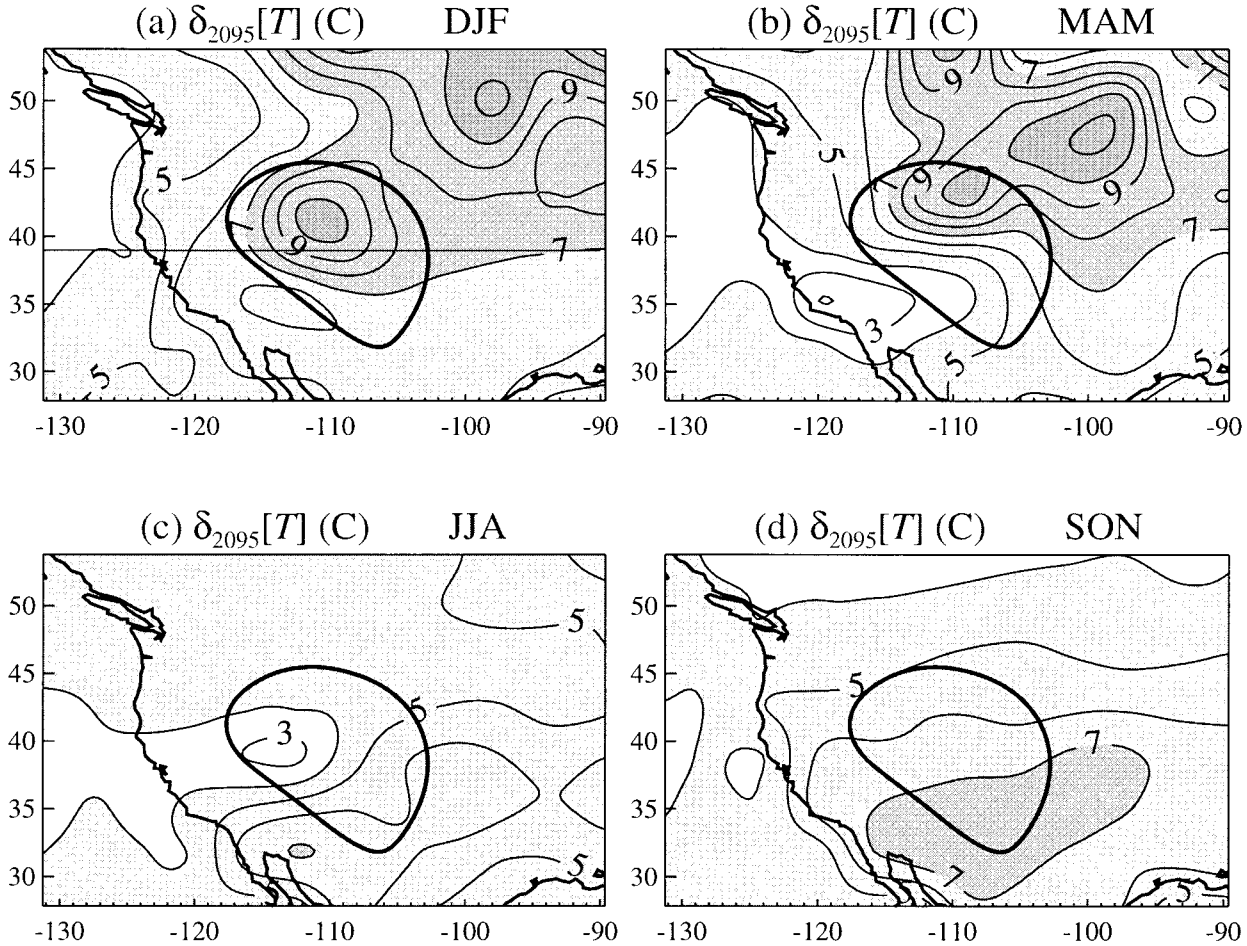


FIG. 3. Screen temperature climate change signal at 2095 (units = °C): (a) DJF, (b) MAM, (c) JJA, (d) SON. The bold curve in each plot is the 1.5-km elevation contour (see Fig. 1b).

over the northwestern slopes of the Rocky Mountains in DJF which is the primary focus of this paper (unless specified assume all subsequent plots are for DJF). Before proceeding we draw attention to the relatively large DJF warming in the northeast sector of domain. This nonlocal continental-scale pattern of warming (seen in many current models) is driven by some of the same mechanisms as the elevation effect but is not directly connected with topography and is not the subject of this investigation.

The diamonds in Fig. 4 display DJF $\delta_{2095}[T]$ at each elevation greater than 1 km. The bold curve was obtained by binning in 250-m intervals. An enhanced climate change signal at high elevations is very apparent. The height of the vertical bars indicate the 99% confidence interval, $\pm 2.4\ \sigma_{2095}[T]$ showing that the enhancement of the climate change signal with increasing elevation is clearly statistically significant. For future reference we note that results for the so-called upper Rockies will often be presented; in these cases we are referring to averages at the four highest points in the domain (yielding, as they do, the four largest climate changes).

Figure 5 displays the time development of the climate change signal (Fig. 5a) and the variability about it (Fig. 5b) along the east–west transect displayed in Fig. 3a. The topography along the transect is plotted under each panel. As can be seen, the enhanced climate change signal (Fig. 5a) appears shortly after the turn of the next century and takes on an increasingly important role thereafter. Note also the relatively small climate change signal on the western side of the Rockies, due, of course, to oceanic thermal inertia.

We now inspect the climate change signal in variables other than screen temperature. Figure 6c displays snow depth $M$ in winter for the reference period (centered on year 1915). In the reference winter the Rockies are laden with snow, leading to the high values of surface albedo $\alpha$ shown in Fig. 6e. Now, looking at the right-hand-side panels in Fig. 6 we conclude that the considerable warming over the Rockies (as noted by the 0° isotherm displacement in Fig. 6b) is associated with vanishing snow

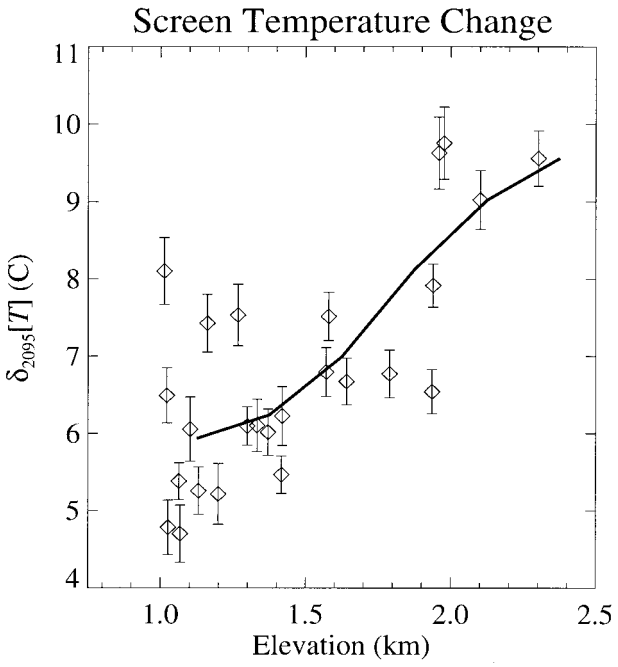


FIG. 4. DJF screen temperature climate change signal at 2095 (units = °C). The curve was obtained by binning in 250-m intervals. The height of the vertical bars represents 2.4 $\sigma[T]$.

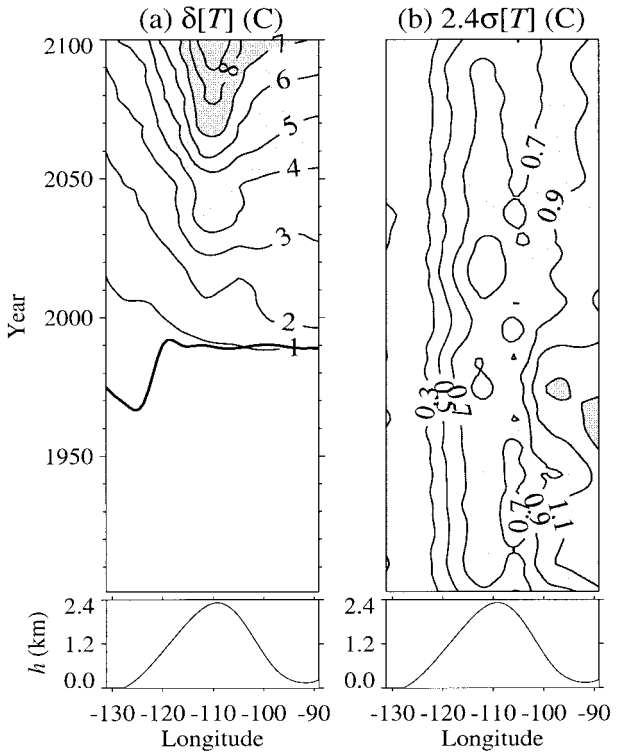


FIG. 5. DJF screen temperature (units = °C). (a) Climate change signal along the east–west transect displayed in Fig. 3a (topography is displayed below). (b) 2.4 times the std dev (topography is displayed below). In (a) the bold curve represents the year at which the climate change signal becomes statistically significant at the 1% level.

cover (Fig. 6d) and plummeting surface albedo (Fig. 6f). We argue that the decreasing surface albedo, due to decreasing snow accumulation, is responsible for amplifying the local temperature response over the Rockies; and in turn, the increasing surface temperature reduces snow accumulation—that is, the snow-albedo feedback. Interestingly, the spatial pattern of warming near the end of the simulations (see Fig. 3a) mirrors the spatial pattern of snow depth at the beginning of the simulations (see Fig. 6c). The initial snow depth controls the difference between snow-covered and bare-ground albedo, and hence the ''amplification potential'' due to the snow-albedo feedback. Where there is little snow to begin with, the snow albedo effect ''saturates'' quickly (i.e., a small temperature increase melts the snow and no further albedo change occurs). Where there is a lot of snow to begin with, the albedo can decrease substantially and so has the potential to significantly amplify the warming.

Figure 7 illustrates the relationship between temperature, snow depth, and albedo more clearly by showing time series of DJF screen temperature change, snow depth, and surface albedo for the upper Rockies (the bold curves). The range of values over points with elevations greater than 1 km is represented with the shading; light (dark) shading implies values greater than (less than) the overall spatial mean. Figure 7a shows that the screen temperature in the upper Rockies begins to rise significantly near the end of this century. Figure 7b shows that the upper Rockies snow accumulation decreases from an average of 60–70 mm (water equivalent) in 1900 to zero by 2100. It is noteworthy that the rate of snow decrease generally accelerates with time (except toward the end of the simulations). Because the surface albedo is a nonlinear function of snow depth, the upper Rockies surface albedo (Fig. 7c) decreases only slightly from 1900 to about 1990 (as highlighted by the horizontal dashed line), but decreases more rapidly thereafter. After the end of this century, the screen temperatures in the upper Rockies increase more rapidly than at lower elevations, leading to a ''fanning out'' of the shaded regions. At the lower elevations, where there is little snow accumulation to begin with, the change in surface albedo is rather modest—the surface albedo is already near the bare ground value. In the upper Rockies, where there is comparatively large snow accumulation at the beginning of the simulation, the albedo reduces by a factor of 2 as the temperature increases and the snow accumulation decreases. The decreasing albedo, due to decreasing snow accumulation, appears to be responsible for amplifying the local temperature response, and in turn, the increasing temperature reduces snow accumulation—again, we identify a snow-albedo feedback where it is the *change* in albedo that is important.

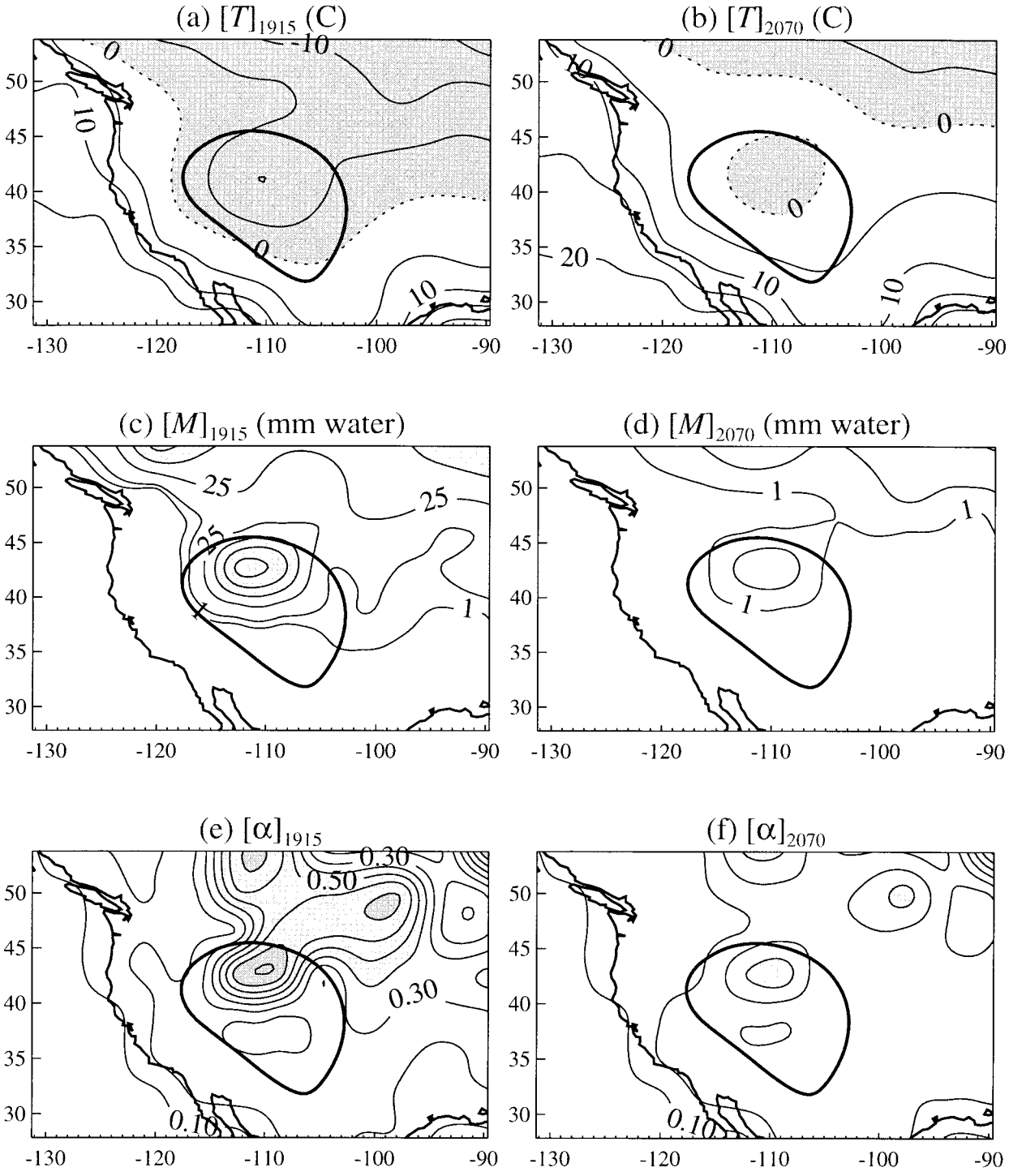


FIG. 6. DJF climate signals. (a) Screen temperature (contour interval = 5°C) at 1915. (b) Screen temperature at 2070. (c) Snow depth (contours at 1, 5, 25, 50, 75, 100, 125, and 150 equivalent mm of water) at 1915. (d) Snow depth at 2070. (e) Surface albedo at 1915. (f) Surface albedo at 2070. The 1.5-km topographic contour (bold) is displayed in all plots.

We now undertake a detailed analysis of the surface energy balance in order to demonstrate the important role of surface albedo changes in the local temperature response.

### *b. The surface energy budget*

The ensemble-averaged surface energy balance for the CCCma Coupled Climate Model can be written as

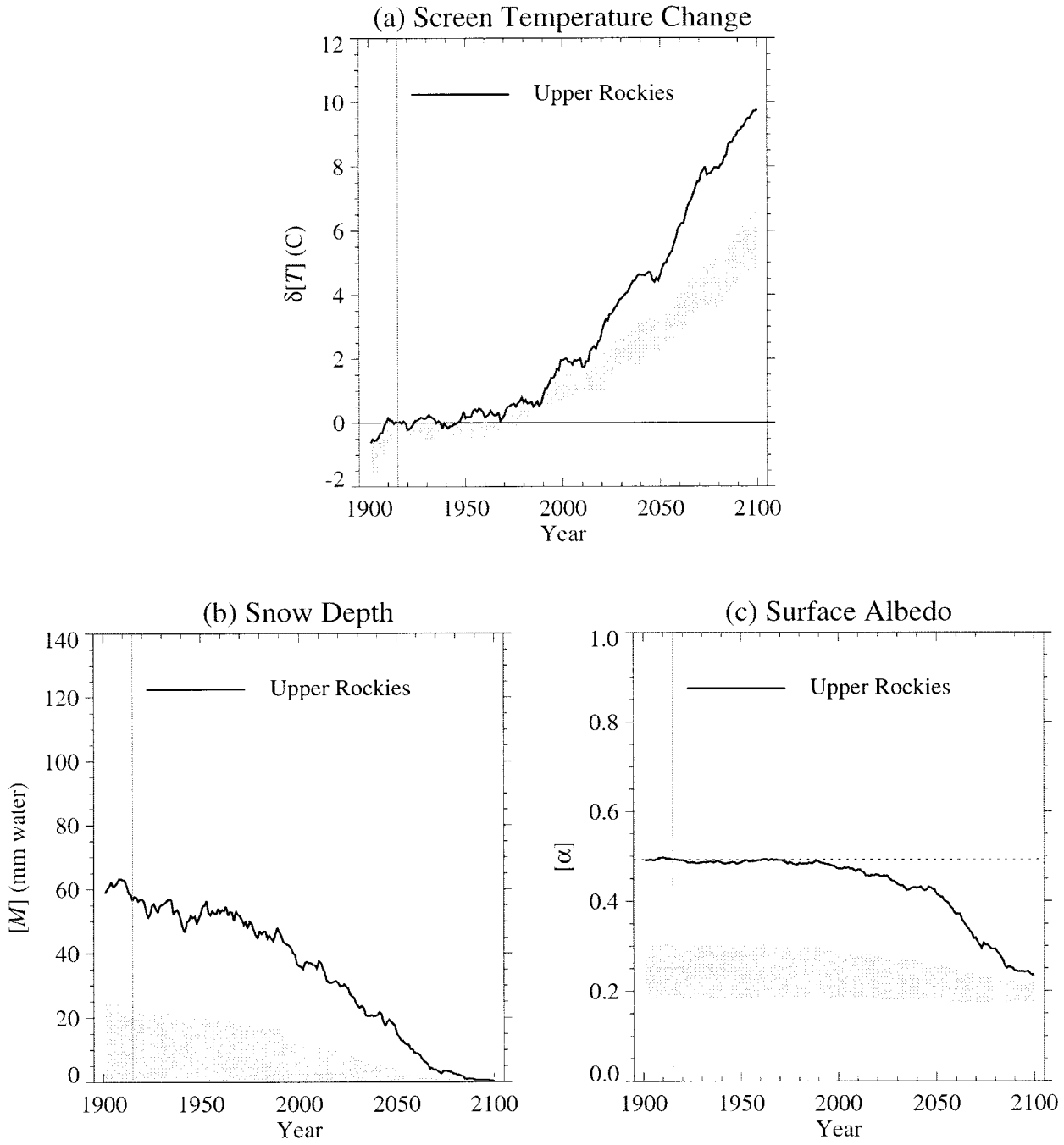


FIG. 7. DJF. (a) Screen temperature climate change signal (units = °C). (b) Snow depth climate signal (equivalent mm of water). (c) Surface-albedo climate signal. In all plots the bold curve is for the upper Rockies and the shading gives the range over all elevations exceeding 1 km: light (dark) shading for values greater than than (less than) the spatial average. The vertical line indicates the reference period. The horizontal dashed line in (c) is drawn at the albedo of the reference period.

$$\left[C\frac{\partial}{\partial t}T^s\right] = [S] + [F] + [L_E] + [H] + L_f[m_F + m_S] + [A], \tag{5}$$

where $C$ is the effective heat capacity of the surface, $T^s$ the surface temperature, $S$ the net solar and $F$ the net infrared radiative flux across the surface, and $L_E$ the latent and $H$ the sensible heat flux. Here $L_f m_F$ represents the melting and freezing of soil moisture or sea ice, $L_f m_S$ represents the melting of snow on land or sea ice, and $A$ represents the transport of energy in the oceans. The quantities on the right-hand side of the equation are

positive (negative) if they represent energy input to (output from) the surface.

From Eq. (5) we write a difference equation in the form

$$\delta[S] + \delta[F] + \delta[L_E] + \delta[H] = \delta[N], \quad (6)$$

where $N$ is a residual term that includes the additional terms in Eq. (5) as well as errors due to round off in the archived data or model inconsistencies, if any (note again that $\delta$ denotes the difference between climate signals at $y_j$ and $y_{j^*}$). Figure 8 displays the DJF average of the terms on the left-hand side of this equation for the upper Rockies over the period $y_j = 2095$. Figures 8a and 8b show that the dominant balance over the Rockies is between changes in solar heating and latent heat cooling, with only small changes in the infrared and sensible heating terms (Figs. 8c and 8d). As an aside we note that the changes over the Pacific Ocean and southwestern United States are largely a balance between increasing infrared and decreasing solar heating. [We also note the similar calculations by Gutowski et al. (1991) for a range of GCMs.]

Clearly, the change in solar radiation is the largest contributor to surface warming over the Rockies. To isolate the cause of this relatively large change we are motivated, as in Boer (1993), to write the solar term in Eq. (6) as

$$\delta[S] = \delta[W] + \delta[C], \quad (7)$$

where $W$ and $C$ are the so-called whitehouse effect and albedo forcing terms, respectively.

#### 1) WHITEHOUSE EFFECT

The ensemble-averaged whitehouse effect is given by

$$[W] = [S_i - S_0], \quad (8)$$

where $S_i$ is the solar flux incident at the surface and $S_0$ the solar flux incident at the top of the atmosphere. This quantity is symmetric with the infrared surface ''greenhouse effect,'' $F_i$ (the incident longwave radiation at the surface), and represents the cooling effect of the atmosphere on the surface in terms of solar radiation. Changes in the cooling effect of the atmosphere compete with albedo forcing changes in determining the new surface energy balance.

#### 2) ALBEDO FORCING

The ensemble-averaged albedo forcing term is given by

$$[C] = [S - S_i] = [-\alpha S_i]. \quad (9)$$

This term is analogous to cloud forcing in the solar and represents the shielding effect of the surface albedo. Importantly, changes in albedo forcing can arise from both surface albedo *and* incident solar radiation changes. To see this we use the right-hand side of Eq. (9) to show that

$$\delta[C] = -S_i^*\delta[\alpha] - \alpha^*\delta[S_i] - \delta[\alpha]\delta[S_i], \quad (10)$$

where $S_i^*$ and $\alpha^*$ are the values of $S_i$ and $\alpha$ for the reference period $y_{j^*}$, respectively.

Figure 8e shows that the albedo forcing change term is large over the Rockies and is in the same sense as the solar radiative change—that is, acting to warm the surface. On the other hand, Fig. 8f shows that the whitehouse effect change opposes the albedo forcing change but not nearly by enough to overcome the latter. We also note that the whitehouse effect term operates in a sense opposite to the infrared change term plotted in Fig. 8c as both changes are due to an increase in cloud over the southwestern portion of the domain. Cloud changes are small over the northern Rockies, and indeed over much of North America, allowing the surface albedo term to dominate.

Finally, comparing Figs. 8g and 8h we conclude that over the Rockies in winter, surface albedo change is mainly responsible for net solar change, which in turn dominates the surface energy balance change—and by implication surface warming. In coming to this conclusion we note that the ''product of changes''—that is, the last term in Eq. (10)—is negligible in these and subsequent calculations.

Figure 9 illustrates the temporal evolution of the various surface energy term changes over the upper Rockies. Figure 9a shows that up until about 2050, latent and sensible heat flux cooling contribute about equally to offsetting radiative warming—which itself comes largely from the solar component (Fig. 9b). We note from Fig. 7c that 2050 is about the time of a precipitous drop in surface albedo. Interestingly, after 2050 changes in sensible heat flux level off, whereas latent heat changes increase in order to keep pace with increasing radiative change (to maintain energy balance). The reason $\delta[L_E]$ continues decreasing after 2050 while $\delta[H]$ does not is unknown at this time but part of the story may involve substantially larger evaporation using energy that may have otherwise gone into sensible heat. The actual reason though is beyond the scope of this paper and will have to await a more complete set of diagnostic variables. The remaining plots in Fig. 9 illustrate again the dominant role of changes in surface albedo (in response to diminishing snow amounts) in setting the surface energy balance, and hence surface temperature over the Rockies in winter. In short, a snow-albedo feedback mechanism is clearly at play in determining the topographically enhanced climate change signal discussed section 3b.

As a final consideration we note that while the snow-albedo feedback might be expected to be largest in March when the sun is the highest in the sky, further analysis (not shown) reveals that the actual warming signal over the Rockies peaks in DJF (as opposed to, e.g., in January–March or February–April).

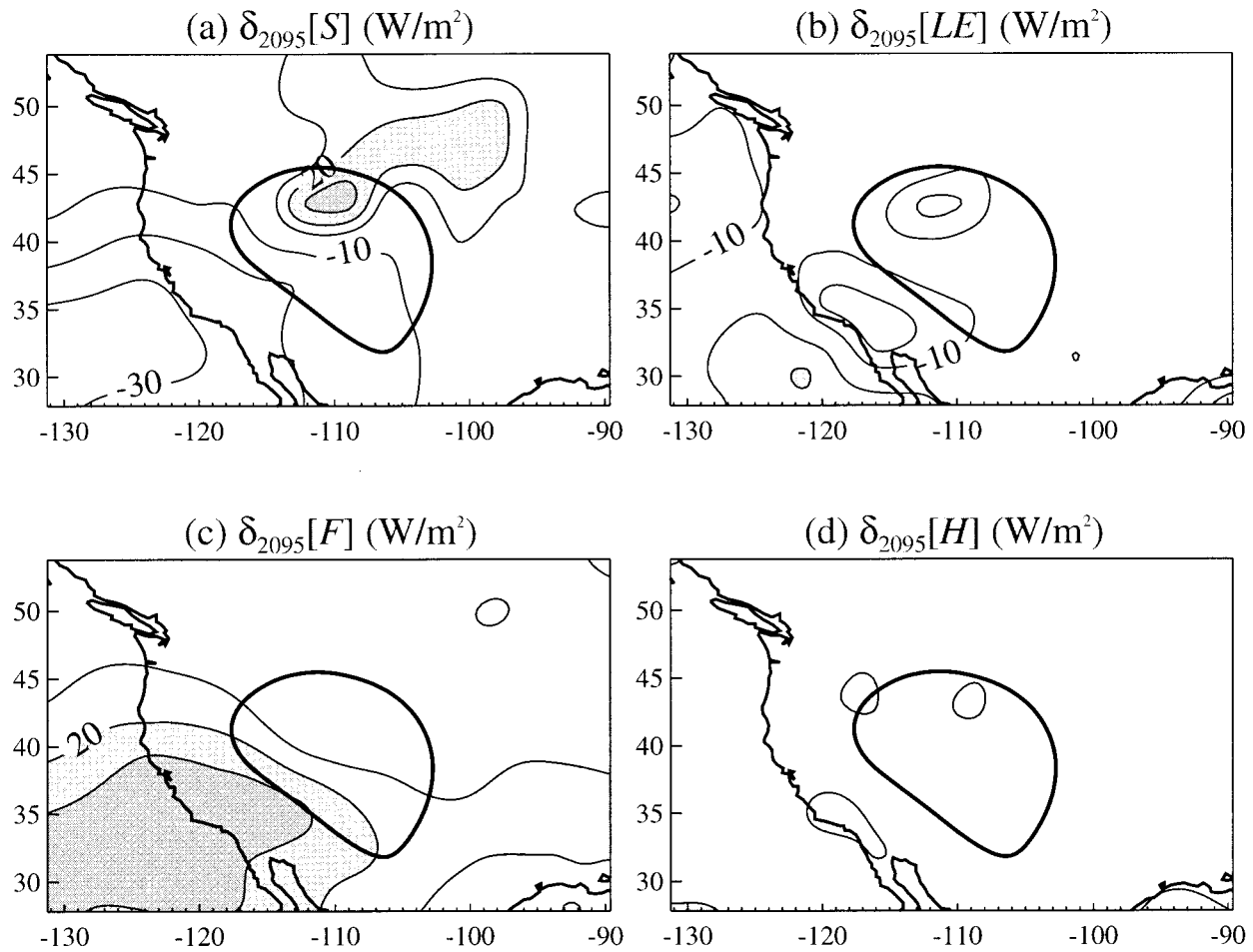


FIG. 8. DJF surface energy balance change (units = W m$^{-2}$). (a) Net solar. (b) Latent heat flux. (c) Net infrared. (d) Sensible heat flux. (e) Albedo forcing. (f) Whitehouse effect. (g) Albedo feedback term. (h) Incident solar feedback term. The 1.5-km topographic contour (bold) is displayed in all plots. The zero contours are omitted.

### *c. Does the enhanced climate change signal imply early detection?*

GHMB suggest that enhanced high elevation temperature change during winter and spring could be used as an early detection tool for global warming. This suggestion ignores the possibility that the high elevation temperature change, while relatively large, may be no more *statistically* significant than a smaller change at low elevation—and hence no more useful for early detection. Referring back to Fig. 5a, we have plotted, as the bold curve, the year at which $\delta[T] > 2.4 \cdot \sigma[T]$ for all subsequent years—or in other words, the period at which the climate change signal becomes forever statistically significant (at the 1% level). We see that the climate change signal is detectable earliest in the maritime region, despite the relatively small signal there. Equally interesting is the fact that the warming signal over the Rockies is not detectable any earlier than that over the lower elevation central continent, despite the eventual amplification of the signal at high elevations. These results are due to the fact that the larger signals are associated with larger variability (as shown Fig. 5b) and so are more difficult to detect. In this subsection we explore in more detail the potential of using high elevations for early climate change detection.

We define the ''detection year'' $y_d$ as the middle year at which all subsequent climate change signals are significant at the $\eta = 1\%$ level. Figure 10a (bold curve) displays the DJF climate change signal for the highest point in the Rockies. The shaded region is the area between the $\pm t_{\eta/2,2I(K-1)}\sigma[T]$ curves. According to the test procedure described in section 2b, we accept the climate change signal as being statistically significant when the bold curve lies outside the shaded area. The DJF detection year is 1989. Figure 10b repeats the calculation for JJA. The JJA detection year is 1992. Although the climate sensitivity is much smaller in JJA than in DJF, the detection year is about the same because of its rel-

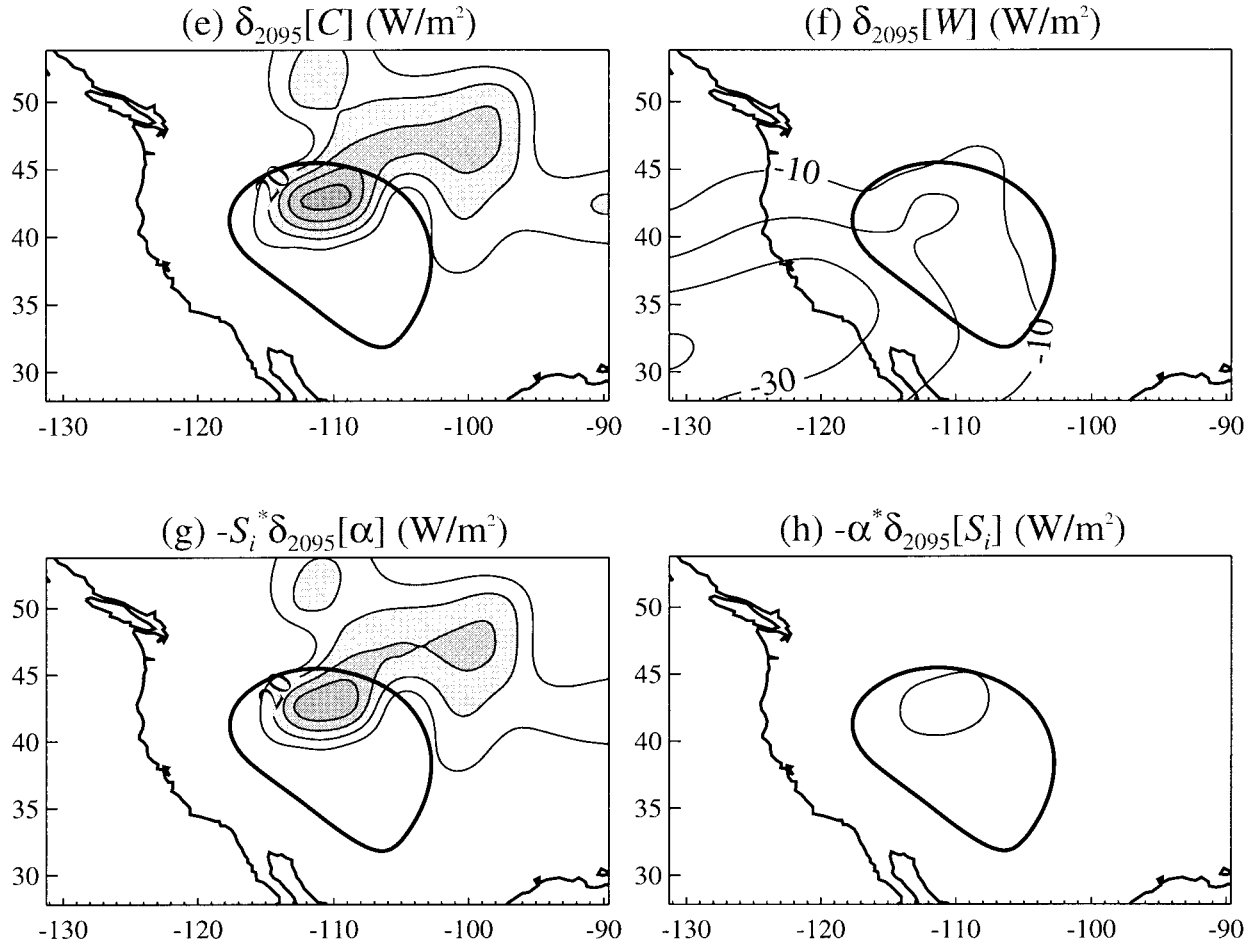


FIG. 8 (*Continued*)

atively lower interannual variability. Large climate change does not necessarily imply early detection.

Another approach to testing the equality of means is the analysis of variance. As we will see, this approach yields essentially the same end result as above but in a way more naturally suited to the treatment of an *ensemble* of means (and is more easily generalized if need be). Very briefly then, the approach begins by noting that the total variance can be partitioned as

$$\sum_i \sum_j \sum_k [(T_{ijk} - \overline{T}_{...})^2 = \sum_i \sum_j \sum_k [(T_{ijk} - \overline{T}_{ij.})^2 + (\overline{T}_{.j.} - \overline{T}_{...})^2 + (\overline{T}_{ij.} - \overline{T}_{.j.})^2]. \quad (11)$$

Next, it is assumed that the data fits the linear statistical model $T_{ijk} = \mu + \alpha_i + \beta_j + \gamma_{ij} + \varepsilon_{ijk}$, where $\mu$ is the grand mean, $\alpha_i$ the ''run effect'' (assumed zero), $\beta_j$ the ''period effect,'' $\gamma_{ij}$ the ''interaction term,'' and $\varepsilon_{ijk}$ a random error component. In statistical language this is a two-way analysis of variance with interaction where one of the main ''fixed'' effects (i.e., the run effect) is assumed zero because all the runs were performed on the same computer, using the same model, the same forcing, etc. Consideration of the distributional properties of the sums of squares in Eq. (11), under the linear statistical model assumption, leads to our alternate test statistic:

$$F_0[T] = \mathrm{MS_P}/\mathrm{MS_E}, \quad (12)$$

where

$$\mathrm{MP_P} = IK \sum_j (\overline{T}_{.j.} - \overline{T}_{...})^2$$

and

$$\mathrm{MS_E} = \frac{1}{2I(K-1)} \sum_j \sum_i \sum_k (T_{ijk} - \overline{T}_{ij.})^2.$$

Here, $\mathrm{MS_P}$ is the ''mean sum of squares'' due to the period effect (with 1 degree of freedom), and $\mathrm{MS_E}$ is the mean sum of squares due to error [with $2I(K-1)$ degrees of freedom]. For our specific purposes we set $j \in [j, j^*]$ in Eq. (12), where $j$ is some arbitrary period whose climate signal we are comparing with the fixed reference period $j^*$.

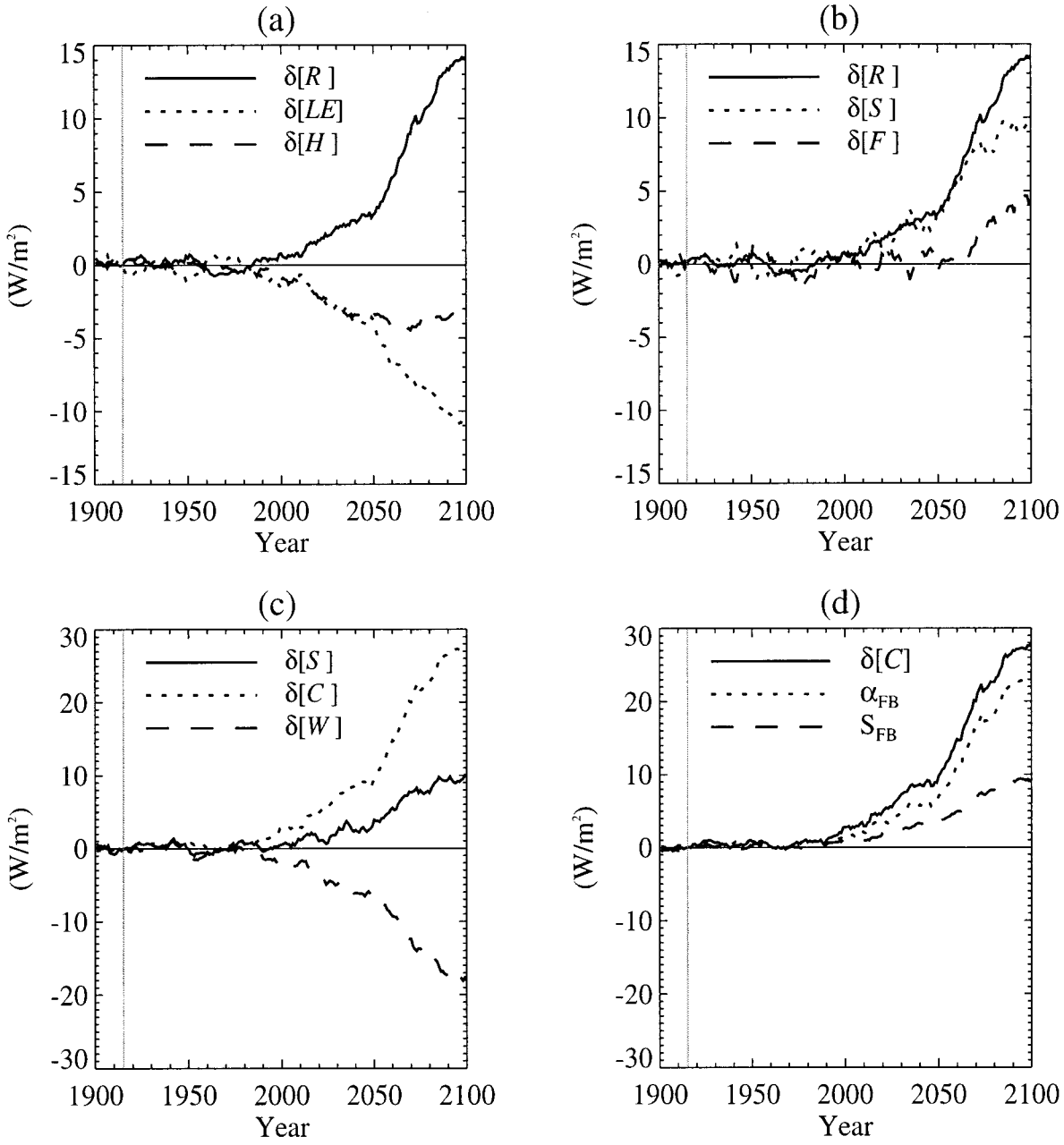


FIG. 9. DJF surface energy balance change for the upper Rockies (units = W m$^{-2}$). See Fig. 8 for a definition of terms. In (a) and (b), $\delta[R] = \delta[S] + \delta[F]$; in (d) $\alpha_{FB} = -S_i^* \delta[\alpha]$ is the albedo feedback term and $S_{FB} = -\alpha^* \delta[S_i]$ is the incident solar feedback term. The vertical line indicates the reference period.

With the $F_0$ test statistic we are attempting to answer the question: Is the variance between periods greater than the variance within periods? The answer being true if $F_0 > F_{\eta,1,2I(K-1)}$, where $F_{\eta,1,2I(K-1)}$ is the percentage point of the $F$ distribution with 1 and $2I(K-1)$ degrees of freedom. As it happens, $F_0 = t_0^2$ and $F_{\eta,1,2I(K-1)} = t^2_{\eta/2,2I(K-1)}$ so that this test procedure and the previous one based on the $t$ statistic are equivalent. In the case of this procedure, however, we have the very useful interpretation of $F_0 - 1$ as a signal-to-noise ratio, $MS_P - MS_E$ being signal and $MS_E$ noise. Figures 10c and 10d (bold curves) display the signal-to-noise ratio at the highest point in the Rockies for DJF and JJA, respectively. Where the bold curves rise above the horizontal line [at $F_0 - 1 = (2.4)^2$] the signal significantly exceeds the noise for that season. We see that because of similar signal-to-noise profiles the DJF and JJA detection years are about the same. In short,

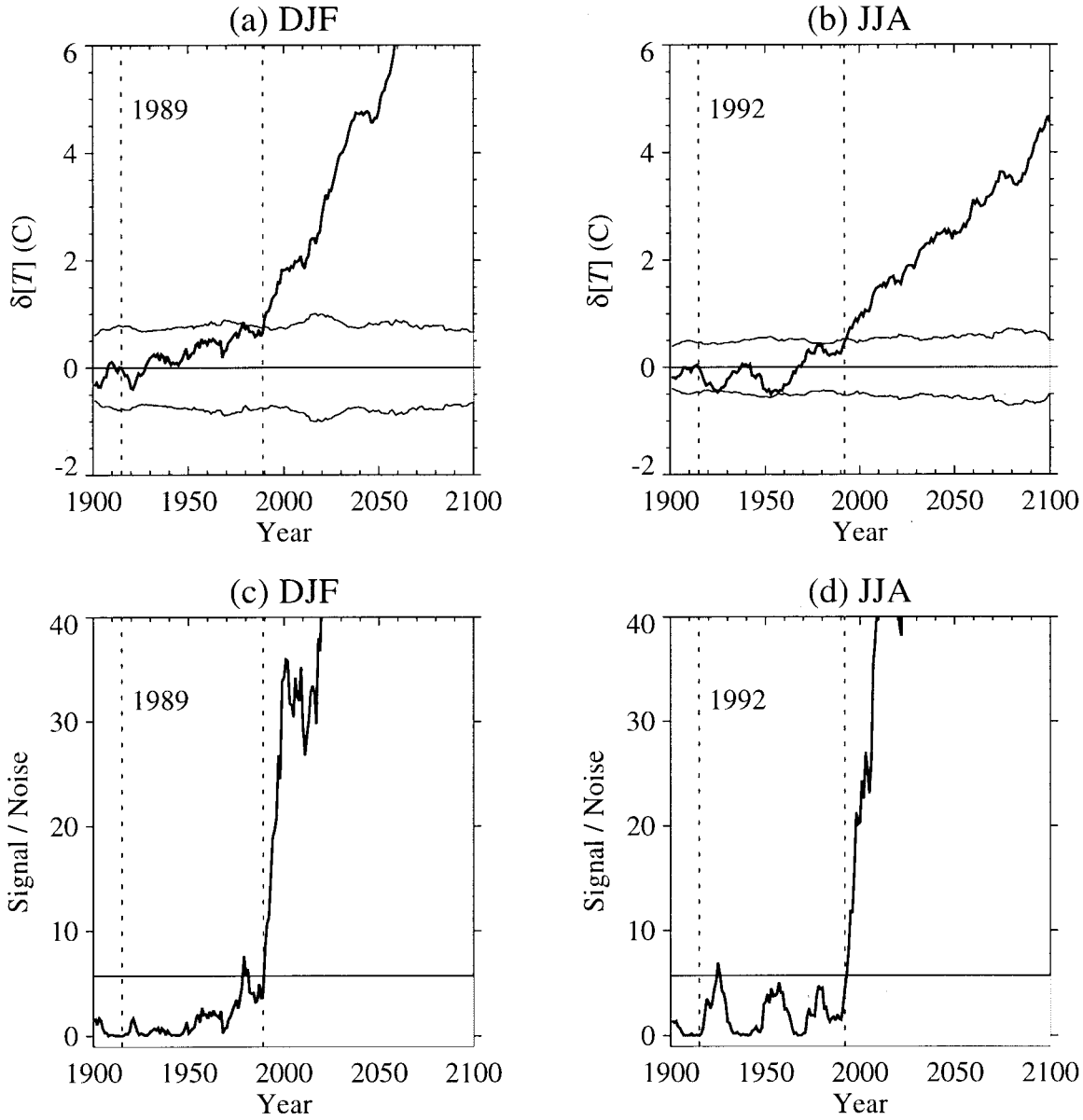


FIG. 10. Upper Rockies. (a) DJF screen temperature climate change signal (units = °C). The shaded region is the area between the $\pm t_{\eta/2,2I(K-1)}\sigma[T]$ curves. (b) As in (a) but for JJA. (c) DJF screen temperature signal-to-noise ratio (i.e., $F_0 - 1$). The shaded region is where $F_0 - 1 \leq (2.4)^2$. The right-most vertical dashed line indicates the ''detection year'' (also printed in the top left corner). The left-most vertical line indicates the reference period.

the climate change signal is only marginally more detectable in DJF than JJA.

Finally, in Fig. 11a we show the spatial distribution of the DJF detection year. We see early detection years over the ocean where, although the climate change signal is low, so too is the noise. Over land no one region is especially favored in terms of early detection. The upper Rockies, in particular, are no more valuable in terms of early detection than any other region over the western part of the continent. Figure 11b shows the climate change signal observed at the detection year. As can be seen there is some enhancement of the climate change signal over the Rockies at the time of detection but even so the signal is no more detectable. Evidently the earliest detectable signal is associated with nonlocal continental-scale warming arising from the ''blanketing'' effect of the increased carbon dioxide.

## 4. Summary and discussion

This study shows that the CCCma Coupled Climate Model exhibits an elevation dependency in surface cli-

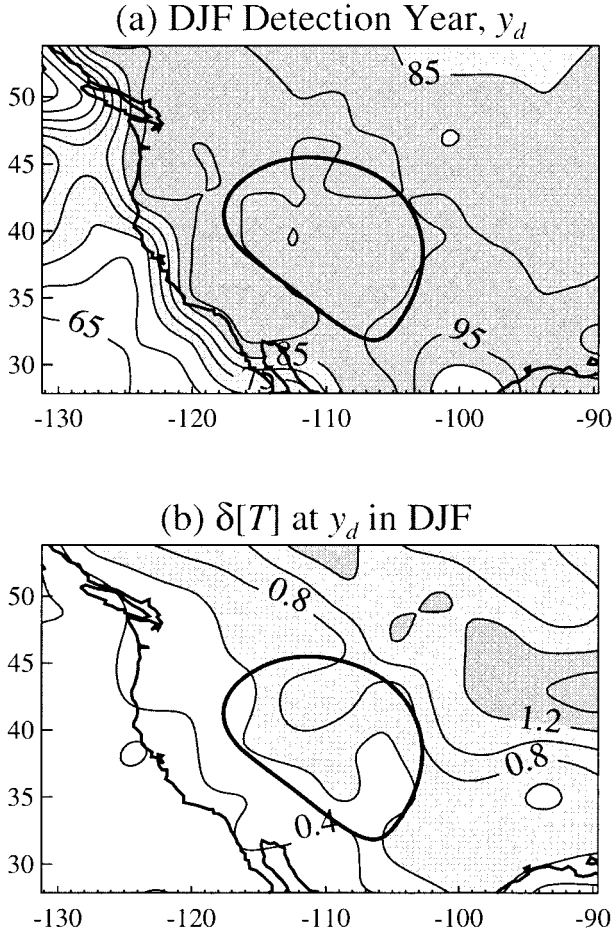


FIG. 11. DJF screen temperature. (a) Detection year (from 1900, contour interval = 5 yr). (b) Climate change signal at the detection year (contour interval = 0.2°C).

mate change in the winter and spring seasons. The elevation signal is due to the reduction of mountain snowpack in the winter and spring seasons and the amplifying effect of the snow-albedo feedback. These results add to and complement the Alpine regional climate model study of GHMB. Not only is the elevation effect shown to exist in a GCM but it is shown to exist in a fully coupled atmosphere–ocean GCM under a reasonably realistic increasing carbon dioxide and aerosols scenario, and where the statistical advantage of an ensemble of long transient simulations is taken.

The primary analysis variable in this study was DJF screen temperature. Other variables, such as winter snow depth and surface albedo, pointed to snow-albedo feedback as the underlying mechanism for the elevation effect. Analysis of the surface energy budget showed that large changes in the solar component of the radiative input were a direct consequence of surface albedo changes caused by decreasing snow cover.

Another of our main results is that the DJF surface temperature change over the Rockies, despite its ultimate amplification as the climate warms, is no more useful for *early* detection than the lower elevation regions. The reason for this is that the topographically enhanced climate change signal is masked by a corresponding increase in variability about that signal. In other words, the signal-to-noise ratio is about the same at high elevations as it is at low elevations. Although the elevation effect eventually dominates the pattern of climate change over western North America, it does so only after the occurrence of considerable continental-scale, detectable warming. As a cautionary note we point out that these results are specific to the Rocky Mountains, a particular model and a specific forcing scenario (although there is no obvious reason why the results would differ for other mountain regions).

Finally, we concur with GHMB that the issue of elevation dependency of the surface climate change signal is an important one for several reasons including the fact that high elevation changes may imply greater impacts on mountain ecosystems and hydrologic systems. As for future work we are exploring the possibility of utilizing the Canadian regional climate model, with its highly sophisticated land surface package, to explore in more detail the elevation signal over the Canadian Rockies (in comparison to the available station data for the region).

*Acknowledgments.* We thank Francis Zwiers and George Boer for helpful review comments on an earlier version of this manuscript, and Dave Ramsden for assembling the model time series files. Special thanks go to both reviewers, particularly for their help understanding certain aspects of the surface energy budget described in section 3b.

## REFERENCES

Beniston, M., and M. Rebetez, 1996: Regional behavior of minimum temperatures in Switzerland for the period 1979–1993. *Theor. Appl. Climatol.,* **53,** 231–244.

Boer, G. J., 1993: Climate change and the regulation of the surface moisture and energy budgets. *Climate Dyn.,* **8,** 225–239.

——, N. A. McFarlane, and M. Lazare, 1992: Greenhouse gas-induced climate change simulated with the CCC second generation general circulation model. *J. Climate,* **5,** 1045–1077.

Giorgi, F., J. W. Hurrel, M. R. Marinucci, and M. Beniston, 1997: Elevation dependency of the surface climate change signal: A model study. *J. Climate,* **10,** 288–296.

Gutowski, W. J., D. S. Gutzler, and W. Wang, 1991: Surface energy balances of three general circulation models: Implications for simulating regional climate change. *J. Climate,* **4,** 121–134.

Langner, J., and H. Rodhe, 1991: A global three-dimensional model of the tropospheric sulfur cycle. *J. Atmos. Chem.,* **13,** 225–263.

McFarlane, N. A., G. J. Boer, J.-P. Blanchet, and M. Lazare, 1992: The Canadian Climate Centre second generation general circulation model and its equilibrium climate. *J. Climate,* **5,** 1013–1044.

Mitchell, J. F. B., T. C. Johns, J. M. Gregory, and S. F. B. Tett, 1995: Climate response to increasing levels of greenhouse gases and sulphate aerosols. *Nature,* **376,** 501–504.

Pacanowski, R. C., K. Dixon, and A. Rosati, 1991: The GFDL modular ocean model user guide. The GFDL Ocean Group Tech. Rep. 2, Geophysical Fluid Dynamics Laboratory, Princeton, NJ, 46 pp.

Reader, C. M., and G. J. Boer, 1998: The modification of greenhouse gas warming by the direct effect of sulphate aerosols. *Climate Dyn.,* **14,** 593–607.

Wilson, M. F., and A. Henderson-Sellers, 1985: A global archive of land cover and soils data for use in general circulation climate models. *J. Climatol.,* **5,** 119–143.